Biomechanics and Modeling in Mechanobiology
https://doi.org/10.1007/s10237-018-1040-9

ORIGINAL PAPER

Simulated tissue growth for 3D printed scaffolds

Paul F. Egan[1] · **Kristina A. Shea**[1] · **Stephen J. Ferguson**[1]

Received: 25 November 2017 / Accepted: 28 May 2018

Abstract
Experiments have demonstrated biological tissues grow by mechanically sensing their localized curvature, therefore making geometry a key consideration for tissue scaffold design. We developed a simulation approach for modeling tissue growth on beam-based geometries of repeating unit cells, with four lattice topologies considered. In simulations, tissue was seeded on surfaces with new tissue growing in empty voxels with positive curvature. Growth was fastest on topologies with more beams per unit cell when unit cell volume/porosity was fixed, but fastest for topologies with fewer beams per unit cell when beam width/porosity was fixed. Tissue filled proportional to mean positive surface curvature per volume. Faster filling scaffolds had lower permeability, which is important to support nutrient transport, and highlights a need for tuning geometries appropriately for conflicting trade-offs. A balance among trade-offs was found for scaffolds with beam diameters of about 300 μm and 50% porosity, therefore providing the opportunity for further optimization based on criteria such as mechanical factors. Overall, these findings provide insight into how curvature-based tissue growth progresses in complex scaffold geometries, and a foundation for developing optimized scaffolds for clinical applications.

1 Introduction

Advances in additive manufacturing are enabling the development of complex, customized designs well suited for biomedical applications (Thompson et al. 2016; Kang et al. 2013). Tissue scaffolds, for instance, potentially benefit from beam-based 3D printed geometries that enable high mechanical efficiency while providing an optimized biological niche (Hollister et al. 2015; Arabnejad et al. 2016). Determining favorable scaffold trade-offs is challenging due to the large number of potential configurations. Additionally, there is limited knowledge in quantifying how a scaffold's structural properties influence the mechanical and biological behavior of cells that colonize a scaffold surface and form tissues that fill the void volume (Egan et al. 2017; Taniguchi et al. 2016). Advances in understanding how tissues grow on varied geometries can lead to improved strategies for scaffold design and optimization. For instance, increasing scaffold surface area is often assumed to increase initial tissue volume and growth, but tissue growth models suggest these surfaces should also have concavity to facilitate faster growth (Bidan et al. 2012, 2013; Guyot et al. 2014; Buenzli 2016; Vassaux and Milan 2017). Here, we develop a computational approach for simulating tissue growth on diverse 3D printed scaffolds, by modeling how tissues grow through mechanically sensing the curvature of a complex three-dimensional scaffold geometry. The purpose of the study is to investigate how tissues grow on 3D printed beam-based topologies, characterize trends relating scaffold geometry to tissue growth, and highlight key trade-offs for optimized scaffold performance.

There is a need for computational methods and mechanobiological models that support automated scaffold configuration since design specifications vary based on in vivo location, targeted tissue type, and patient specific constraints (Carlier et al. 2015). Bone tissue scaffolds are typically designed with structural properties similar to trabecular bone, with pore sizes of 200–800 μm and porosities of 50–80% (Fyhrie et al. 1993; Sanz-Herrera et al. 2008). 3D printing provides an opportunity for generating customized structures, such as beam-based lattices, that have properties similar to bone and potentially better mechanical efficiency for a given porosity (Wang et al. 2016; Melchels et al. 2010; de Wild et al. 2016). As lattice design parameters are altered, scaffolds achieve different relative trade-offs in conflicting properties. For instance, scaffolds with higher porosity have a greater void volume for tissue growth, but reduced mechan-

Electronic supplementary material The online version of this article (https://doi.org/10.1007/s10237-018-1040-9) contains supplementary material, which is available to authorized users.

✉ Paul F. Egan
paul.egan.phd@gmail.com

[1] ETH Zurich, Zurich, Switzerland

Published online: 06 June 2018

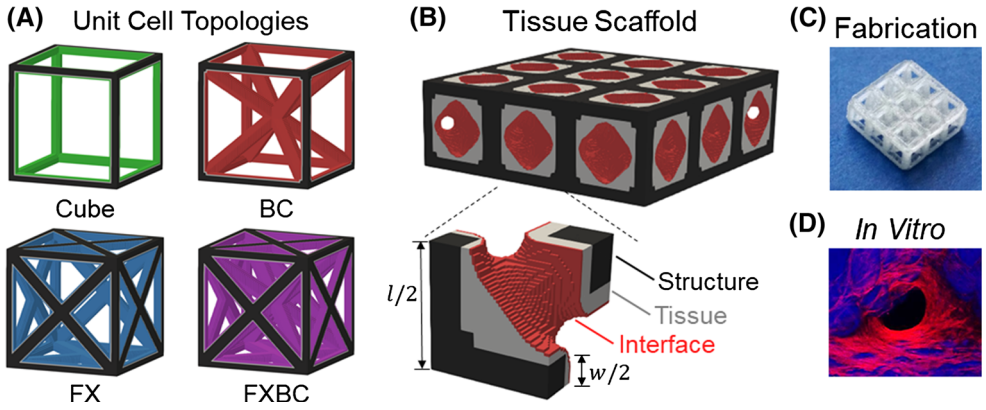

Fig. 1 **a** Complex beam-based unit cell topologies. **b** Tissue scaffold with BC unit cells of length l and beam width w for tissue growth simulations using a voxel environment that tracks structure, tissue, and surface interface. **c** 3D printed scaffold. **d** Representative in vitro growth after five weeks for an FXBC scaffold with 500 μm planar pores and beams with $w = 500$ μm.

ical properties; scaffolds with higher surface–volume ratio have an increased seeded tissue volume, but decreased permeability for nutrient transport (Egan et al. 2017; Vossenberg et al. 2009). Computational approaches enable comparisons of diverse designs, making it possible to identify favorable trade-offs when considering tissue growth within a complex 3D geometry.

Predicting tissue growth from scaffold properties is challenging due to numerous influential factors including mechanostimulation, fluid shear stress, and substrate curvature (Guyot et al. 2016a; Bischofs and Schwarz 2003; Papachroni et al. 2009; Worley et al. 2013; Zadpoor 2015; Sanz-Herrera et al. 2009; Vetsch et al. 2016; Bael et al. 2012; Joly et al. 2013; Knychala et al. 2013; Zhao et al. 2015). Curvature-based models have been validated through in vitro experiments and assume tissue growth is proportional to the concavity of a tissue front; no tissue growth occurs on flat or convex surfaces (Bidan et al. 2012, 2013; Guyot et al. 2014; Bidan et al. 2013; Rumpler et al. 2008; Alias and Buenzli 2017). Recently, in vivo experiments have demonstrated curvature-driven growth in an ovine model that resulted in seamless integration of soft tissue into newly formed bone (Paris et al. 2017). Curvature is typically calculated using level set methods (Guyot et al. 2014) or via a scanning mask in a voxel environment (Bidan et al. 2013). These approaches are extendible to include further factors influencing tissue growth, such as fluids models to calculate shear stress (Guyot et al. 2016b). Curvature-based evaluations are well suited for systematic analyses of diverse scaffold geometries since they provide an efficient initial approximation for identifying designs with potentially high tissue growth rates (Fig. 1; Supplementary Movie 1).

Beam-based lattices consist of unit cells with varied beam topologies (Fig. 1a) patterned to form tissue scaffolds (Fig. 1b) that are 3D printed (Fig. 1c) and suitable for in vitro cell culture testing (Fig. 1d) (Egan et al. 2017). Unit cells of varied topologies differ in their mechanical properties as well as interconnectivities among pores of varied shapes (Fig. 1a). Tissue growth is efficiently simulated by generating a voxel structure and tracking the interface of tissue and void space, by assuming the interface advances proportional to its local positive curvature (Fig. 1b). Diverse scaffold designs are configured using two independent design parameters of beam width w and unit cell length l that enable calculation of geometrically based scaffold properties including porosity, pore size, surface–volume ratio, and permeability (Egan et al. 2017). Numerous 3D printing processes are available for manufacturing beam-based scaffolds, including the polyjet printing process used to fabricate samples using a biocompatible polymer (Fig. 1c). Only a portion of the scaffold requires simulation, when assuming simulations represent an average growth measured from many stochastic tissue growth experiments, as illustrated by Saos-2 growth in Fig. 1d. Saos-2 cells are a human osteosarcoma cell line that are experimentally well characterized, widely available, and have osteoblastic features (Rodan et al. 1987; Sobral et al. 2011) that make them well suited for in vitro evaluation of tissue growth relevant to bone tissue engineering applications.

The first step in our approach is to determine how three-dimensional beam-based geometries influence tissue growth in comparison with past models assessing three-dimensional structures with complex surfaces with no beams (Bidan et al. 2013). Unit cell design parameters are then varied to generate diverse scaffolds with fixed properties for quantifying modeling trends. These trends inform efficient optimization by using statistical regression to approximate simulation results with analytical equations (Egan et al. 2015, 2016). Trends are then used to evaluate opposing scaffold design trade-offs, namely tissue growth rates being higher for smaller pores while permeability is lower (Kang et al. 2013). The approach aims to provide significant advancements for understanding tissue growth in complex geometries while also producing predictive models to facilitate scaffold optimization for clinical applications.

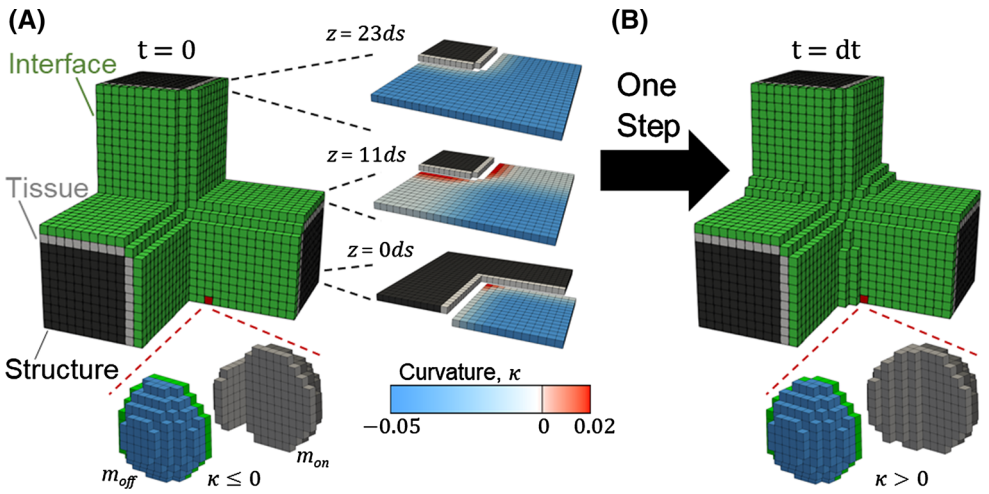

Fig. 2 **a** Discretized Cube corner with beam width $w = 200\,\mu\text{m}$, unit cell length $l = 500\,\mu\text{m}$, and spherical scanning mask radius $m_r = 5.5$ ($10\,\mu\text{m}$ voxel length ds). Curvature κ is calculated for each voxel in cross sections with height z. **b** Environment after time step dt. For clarity, void voxels are only rendered in scanning masks

2 Methods

2.1 Design generation

Cubic unit cell topologies were generated by placing voxels to form beams with square cross sections. Only one corner of each unit cell was generated, which represents one-eighth of a unit cell's volume. All topologies shared the same beams that extend along unit cell edges, with the Cube topology consisting of only these beams. The BC topology includes additional beams that extend from the unit cell corner toward the unit cell center, and the FX topology includes beams from each unit cell corner toward the center of each unit cell face, while the FXBC includes both. The smallest pore size and shape are defined as the smallest planar void area for each unit cell topology (Arabnejad et al. 2016). The smallest planar pores for the Cube, FX, and FXBC topologies consist of the smallest square or triangular interconnectivity pore on the face of each unit cell, while the BC topology's smallest pore is based on the triangular cross section that forms between internal beams. Pore size is calculated based on the remaining planar area without tissue, therefore it is largest initially prior to tissue seeding and decreases in size as tissue is seeded and grows to fill the scaffold.

2.2 Tissue growth simulation

The simulation was developed by extending past approaches using voxel environments for tissue growth on complex surfaces (Bidan et al. 2013) to efficiently simulate tissue growth in complex 3D printed geometries. Each voxel is a discrete cubic volume defined as structure, tissue, interface, or void. Interface voxels are adjacent to tissue voxels and indicate locations on the tissue surface for potential growth and are also considered void since they do not contain structure or tissue. Voxel length ds is based on mask radius m_r (measured as a discrete number of voxels from the mask center) and cell reach c_r (measured as continuous units from the mask center) of growing tissue to mechanically sense their surrounding environment such that

$$\text{ds} = \frac{c_r}{m_r} \tag{1}$$

with $c_r = 55\,\mu\text{m}$ held constant (Bidan et al. 2013). Therefore, when $m_r = 5.5$, voxel length ds represents $10\,\mu\text{m}$.

The simulation represents a corner of a unit cell with length l. The voxel environment is $\frac{l}{2 \cdot \text{ds}}$ voxels in x, y, and z directions. Structure voxels are placed to represent beams with square cross-sectional areas of width w. Void voxels adjacent (but not diagonal) to each structure voxel are defined as tissue voxels and void voxels adjacent (but not diagonal) to tissue voxels are defined as interface voxels in time step $t = 0$ (Fig. 2a).

For each voxel mapped with the scanning mask, structure and tissue voxels are counted as substrate m_{on}, while interface and void voxels are counted as empty m_{off}. Voxel curvature is calculated as

$$\kappa = \frac{16}{3 \cdot c_r}\left(\frac{m_{\text{on}}}{m_{\text{on}} + m_{\text{off}}} - \frac{1}{2}\right) \tag{2}$$

by assuming curvature is only positive (i.e., concave) when m_{on} consists of over half the voxels in the scanning mask (Frette et al. 2009; Bullard et al. 1995). The unit cell corner is assumed to be within the interior of the scaffold, with

its boundaries interfacing with another unit cell of identical geometry. When mapped mask voxels extend beyond the voxel environment boundaries, their state is defined by assuming that voxels beyond the boundaries mirror voxel states within boundaries, providing symmetric boundary conditions based on unit cell symmetry. The scanning mask is used to calculate κ for all interface voxels at each time step and voxels with $\kappa > 0$ become tissue in the next time step as the process is repeated (Fig. 2b).

2.3 Computational efficiency

The computation time for a simulation is highly dependent on the number of curvature calculations required (i.e., mask applications). Since only voxels with $\kappa > 0$ change states, it is inefficient to calculate curvature for voxels far away from the interface that are likely to have $\kappa \leq 0$ and remain static. Rather than calculating curvature for all void voxels in the simulation, the simulation method's efficiency is improved by incorporating an iterative search by first calculating κ of all interface voxels, and then calculating κ of all voxels adjacent to voxels with $\kappa > 0$ until all voxels adjacent to voxels with $\kappa > 0$ are found to have $\kappa \leq 0$. When using the iterative search, the number of mask applications for calculating voxel curvature each time step is roughly proportional to the number of interface voxels rather than the number of void voxels. The efficiency increase is dependent on the unit cell design, and the iterative search should decrease computational time proportional to the difference in the number of void voxels to interface voxels per time step, although other factors in coding and hardware may also influence computational time. When $m_r = 5.5$, there are approximately 7 times more void voxels than interface voxels for a Cube with $w = 200$ and $l = 400$ in the first time step, but approximately 175 times more void voxels than interface voxels for a Cube with $w = 200$ and $l = 2000$. When using a 2.4 GHz core, the first time step requires approximately 1.5 s computation for the $l = 400$ Cube with $\sim$500 interface voxels and $\sim$3000 void voxels and approximately 20 s computation time for the $l = 2000$ Cube with $\sim$5500 interface voxels and $\sim$1,000,000 void voxels when using the iterative search method. Simulations were run with python and rendered with ParaView (Liu et al. 2017), and simulations continue until all interface voxels have $\kappa \leq 0$ or no interface/void voxels remain.

Methods were developed for assessing in vitro tissue growth of scaffolds with the same number of unit cells as the designed sample in Fig. 1c. Due to the small size of these samples and their open pores, it is assumed there is adequate nutrition available to all locations in the scaffold, even when nutrient distribution is slowed as planar interconnectivity pores are blocked by growing tissue (Guyot et al. 2015). These assumptions support the choice to only simulate one-eighth of the unit cell structure that is representative of an average stochastic growth, which provides computational efficiency in comparison with simulating the entire scaffold. Constraints are placed on the minimum/maximum dimensions of unit cells to ensure the mask size does not exceed the beam diameter width and the unit cell length does not exceed 2000 μm since unit cells with length greater than 2000 μm generally have pores sizes too large for efficient tissue growth. Beam width is varied from 100 to 1000 μm for simulations, which is representative of achievable dimensions from 3D printing processes that are suitable for bone tissue engineering.

3 Results

3.1 Tissue growth comparisons for 2D, 2.5D, and 3D beam-based geometries

The Cube topology was simulated initially to determine how beams influence growth in comparison with 2D/2.5D geometries with square pores from past studies (Bidan et al. 2013). 2D geometries refer to simulations that are one voxel in height, while 2.5D geometries refer to three-dimensional simulations that extrude the voxels of a 2D geometry into three-dimensional space such that all cross sections at different heights have the same voxel composition initially. 2.5D geometries are evaluated using the same simulation methods as described for 3D beam-based geometries, while the curvature of voxels for 2D geometries is evaluated using a planar circular scanning mask. For consistency with past studies, a mask radius of $m_r = 8.5$ was used initially.

All structures were generated with pore size $p = 500$ μm, with pore size calculated as $p = l - w$ for the Cube. The Cube's beams have width $w = 500$ μm, while unit cell length l is solved. The 2.5D geometry has height equal to its pore size, and the 2D/2.5D geometries have wall widths one voxel larger than m_r. The void proportion filled P_{fill} for each simulation was calculated by counting the total number of voxels v_{tot} where tissue or structure may be placed, total number of structure voxels v_{str}, and total number of tissue voxels v_{tiss} such that

$$P_{fill} = \frac{v_{tiss}}{v_{tot} - v_{str}} \tag{3}$$

and was tracked for simulation renderings in Fig. 3a for each time step t in Fig. 3b (Supplementary Movie 2).

Void space fills fastest for 2D geometries, with renderings demonstrating the circular tissue front that forms as void space linearly fills over time (Bidan et al. 2013). 2.5D and Cube geometries fill at similar rates, with filling occurring slightly faster for the 2.5D geometries in comparison with the Cube until planar pores for both designs close shortly after

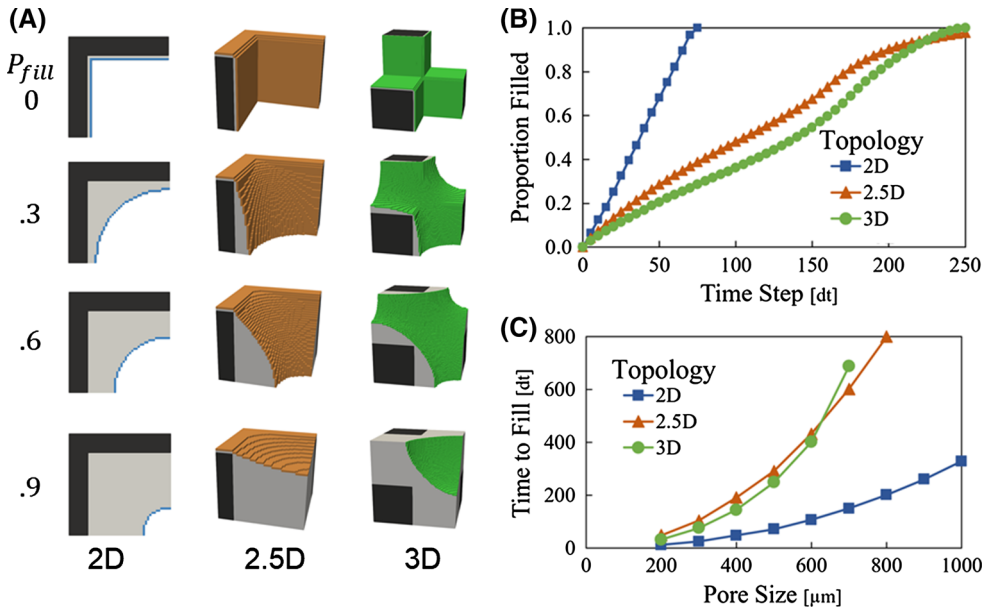

Fig. 3 **a** 2D, 2.5D, and 3D geometries simulated and rendered with proportion filled P_{fill}. **b** P_{fill} for each time step t. **c** Time to fill t_{fill} for structures with pore size p

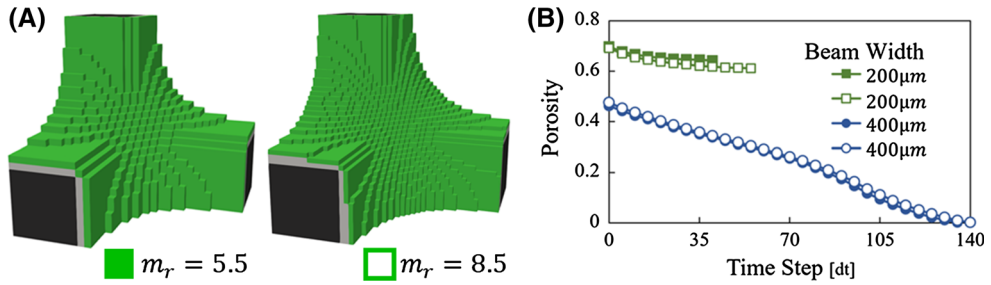

Fig. 4 **a** Converged simulations with halted tissue growth for Cubes with beam width $w = 200\,\mu\text{m}$, unit cell length $l = 600\,\mu\text{m}$, and mask voxel radius m_{r}. **b** Porosity P as a function of time step t, with $w = 400\,\mu\text{m}$ and $l = 800\,\mu\text{m}$ designs; closed symbols denote $m_{\text{r}} = 5.5$, open for $m_{\text{r}} = 8.5$

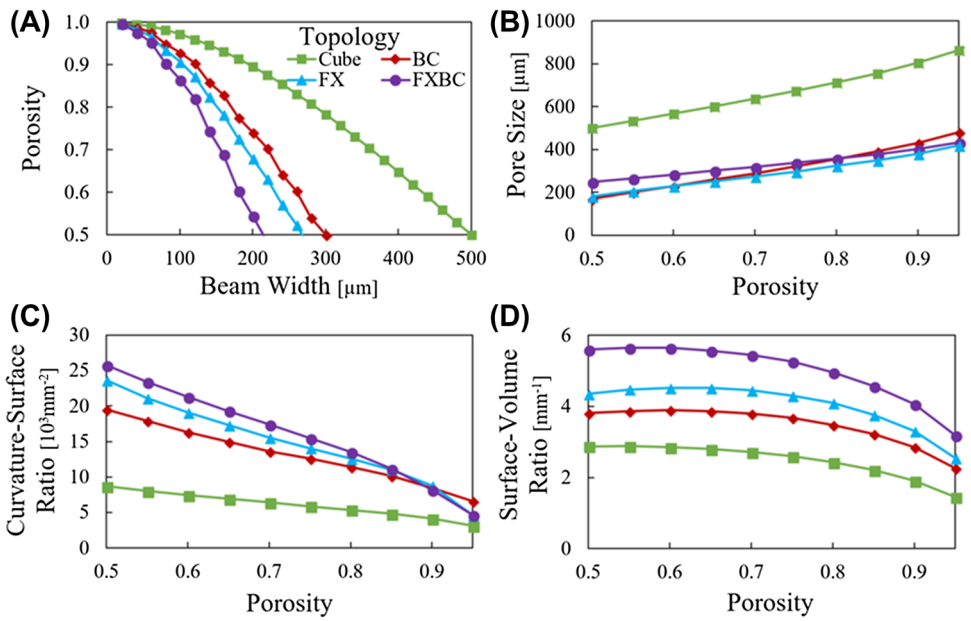

Fig. 5 Topologies with unit cell length $l = 1000\,\mu\text{m}$ as **a** porosity P varies for designs with beam width w. **b** Pore size p, **c** curvature–surface ratio $\overline{\kappa_+}/S$, and **d** surface–volume ratio S/V for varied P

$P_{\text{fill}} = 0.6$ (Note: for the 2.5D geometry, the top layer of the environment is not considered in v_{tot} calculations since it results in a layer of void interface with no tissue growth). For the Cube, growth starts at beam connections and continues until planar pores are closed and a central void emerges. The growth rate changes for these designs once planar pores close, due to the change in curvature relative to the advancing tissue front. A large spherical void emerges for the Cube and a flatter curved surface with a square cross-sectional forms for the 2.5D structure prior to complete void filling.

When p is increased in 100 µm increments while w remains constant, there is an exponential increase in time to fill t_{fill} as p increases (Fig. 3c), where t_{fill} indicates the number of time steps required until $P_{\text{fill}} = 1$. 2.5D structures of $p \geq 800\,\mu\text{m}$ and Cubes of $p \geq 700\,\mu\text{m}$ do not fill completely, as growth is halted because curvature for all void voxels is $\kappa \leq 0$. Halted growth occurs for Cubes with $p \geq 700\,\mu\text{m}$ prior to the growing tissue closing the planar pore as demonstrated in Fig. 4a for structures with $w = 200\,\mu\text{m}$ and $l = 600\,\mu\text{m}$. Masks of $m_{\text{r}} = 5.5$ and $m_{\text{r}} = 8.5$ were used to assess whether resolution influences halting occurrence and tissue growth over time (Christen et al. 2016). Porosity P is based on the total number of voxels v_{tot}, number of structure voxels v_{stru}, and number of tissue voxels v_{tiss} such that

$$P = 1 - \frac{v_{\text{stru}} + v_{\text{tiss}}}{v_{\text{tot}}} \tag{4}$$

and is used to track growth over time in Fig. 4b.

Simulations with the larger mask require slightly more time steps until growth halts and converge with a similar interface geometry and P as simulations with the smaller scanning mask. Simulations were repeated by increasing w and l by 200 µm, therefore generating structures with the same pore size as Fig. 4a designs, but larger beams and lower P that results in complete void filling (Fig. 4b). Mask size has minor influences on outcomes, which motivates the use of $m_{\text{r}} = 5.5$ for all further simulations due to its greater computational efficiency. When comparing findings with Fig. 3c, when $w = 500\,\mu\text{m}$ halting does not occur until $p \geq 700\,\mu\text{m}$, which suggests that the ratio of p to w dictates whether growth completely fills a void, rather than absolute values of p and w.

3.2 Implications for tissue growth for varied 3D beam-based geometries

Geometrical properties for beam-based scaffolds with different topologies were compared with fixed unit cell volumes by increasing beam width w from 20 to 500 µm when unit cell length was held constant at $l = 1000\,\mu\text{m}$. Porosity P is shown to decrease with increasing w for each topology (Fig. 5a). The porosity is evaluated using Eq. 4, with $v_{\text{tiss}} = 0$, such that the porosity refers to that of the designed structure only. If the structures were seeded with tissue, their porosity would slightly decrease since $v_{\text{tiss}} \geq 0$.

For a given w, P is the highest for the Cube, then BC, FX, and FXBC topologies. The Cube topology has significantly higher P for a given w because it has fewer beams per unit cell compared to the other topologies, so their width must be higher to fill the same void space per unit cell. P is then used as an independent variable for comparing scaffold properties of pore size p, curvature–surface ratio $\overline{\kappa_+}/S$, and surface–volume ratio S/V while maintaining unit cell length $l = 1.0$ mm.

Pore size p is found by counting the number of void voxels that make up the smallest planar pore v_{pore} of a unit cell and converting to continuous units with the following equation

$$p = \text{ds} \cdot \sqrt{A \cdot v_{\text{pore}}} \tag{5}$$

using $A = 4$ for the Cube topology, $A = 2\sqrt{2}$ for the BC topology, and $A = 2$ for FX and FXBC topologies. A is adjusted based on the proportion of the pore represented by the corner of the unit cell; the $\sqrt{2}$ adjustment for the BC topology accounts for numerical error due to voxels being arranged on an internal diagonal. In Fig. 5b, p increases for each topology as P increases, with the Cube topology having the highest p at a given P. The remaining topologies have similar values.

Curvature–surface ratio $\overline{\kappa_+}/S$ considers the mean positive surface curvature $\overline{\kappa_+}$ by determining mean κ (Equation 2) for all interface voxels with $\kappa > 0$, then dividing by the total number of interface voxels v_{int} that is used to find the surface area S adjusted to continuous units by $S = v_{\text{int}} \cdot (\text{ds})^2$. The resulting relationship

$$\overline{\kappa_+}/S = \frac{\overline{\kappa_+}}{v_{\text{int}} \cdot (\text{ds})^2} \tag{6}$$

has been suggested in past studies as a predictor of three-dimensional tissue growth rates on complex surfaces (Bidan et al. 2013). In Fig. 5c, $\overline{\kappa_+}/S$ is shown to decrease with increasing P and is lower for the Cube in comparison with the similar values for other topologies, with the FXBC topology having the highest followed by the FX topology.

Surface–volume ratio S/V is determined with the total number of interface voxels v_{int} divided by the total number of voxels v_{tot}, such that

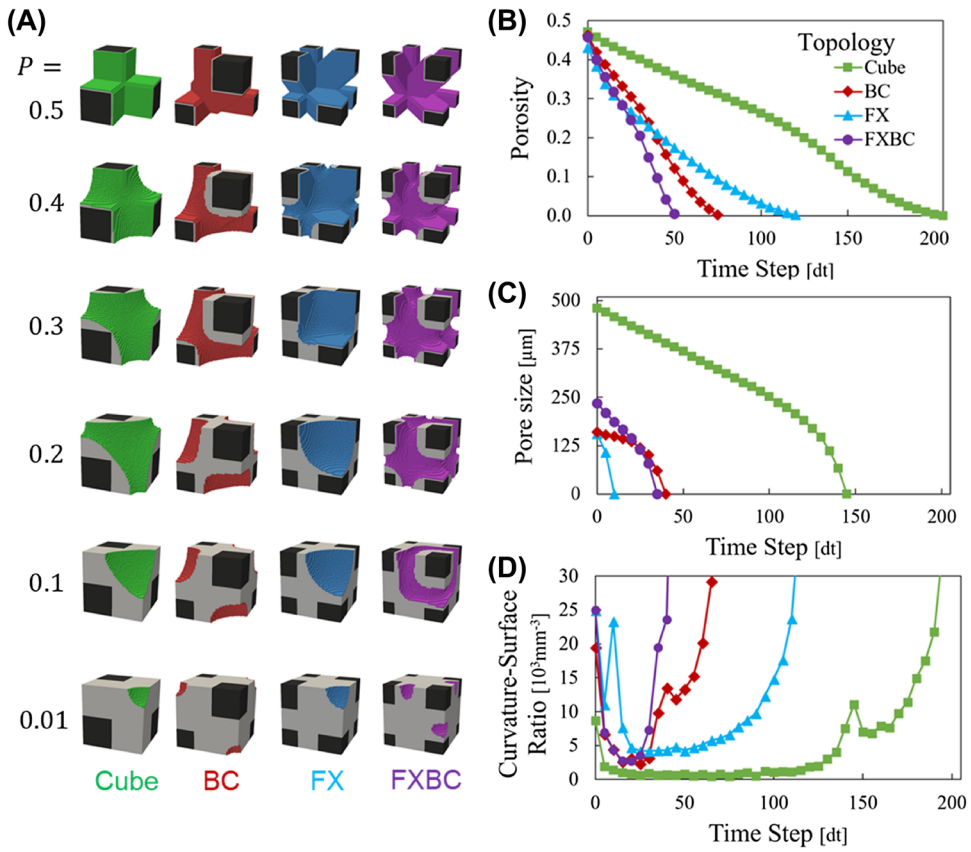

Fig. 6 **a** Simulations rendered with approximate porosity P and unit cell length $l = 1000\,\mu$m. **b** Porosity P, **c** pore size p, and **d** curvature–surface ratio $\overline{\kappa_+}/S$ as a function of time step t

$$S/V = \frac{v_{\text{int}}}{v_{\text{tot}}} \cdot \frac{1}{\text{ds}} \tag{7}$$

where $\frac{1}{\text{ds}}$ is used for unit conversion. In Fig. 5d, all topologies decrease in S/V as P increases, with the FXBC topology having the highest S/V, followed by FX, BC, and Cube topologies for a given P. Nonlinearities in the relationship of surface–volume ratio to porosity suggest that sharper decreases in S/V occur for higher P, notably once $P \geq 0.8$. The absolute amount of seeded tissue for a scaffold is proportional to S/V, which is chosen as an evaluation metric for comparing topologies since it is an intrinsic property that retains its value as a unit cell is patterned to form a larger scaffold volume (Egan et al. 2017).

3.3 Tissue growth comparisons for varied 3D geometries

Controlled comparisons of tissue growth over time are conducted for scaffolds in Fig. 5 with $P = 0.5$. Renderings were generated at regular intervals of P, in addition to tracking P, p, and $\overline{\kappa_+}/S$ for each time step t in Fig. 6 (Supplementary Movie 3).

In comparison with the Cube topology where tissue forms one large central closed pore, tissue in the BC topology forms three internal voids once internal interconnectivity pores are closed. For the FX and FXBC topologies, the pores on the unit cell face initially close, resulting in one large void for the FX Cube while the FXBC topology then forms three voids, similar to the BC topology.

Growth relates directly to quantitative tracking of properties over time, with growth occurring at different rates over time for each topology (Fig. 6b). The rate depends on initial surface–volume ratio and how soon pores close (Fig. 6c), which influences the curvature–surface ratio that dictates how fast a tissue front advances (Fig. 6d). Porosity decreases fastest for FX and FXBC topologies initially in Fig. 6b, but once their initial pore is filled, as indicated in Fig. 6c, tissue growth slows considerably for the FX topology since one large central void forms whereas the growth remains fast for the FXBC topology due to its diagonal beam element. Growth of the BC topology then surpasses the FX topology, while the Cube topology consistently has the slowest growth. When pores fill (Fig. 6c), there is a temporary increase in curvature–surface ratio (Fig. 6d) that is expected, since more voxels with higher positive curvature are concentrated in a smaller surface area in the closing pores. The curvature–surface ratio increases the rate of tissue growth for the scaffolds, which suggests for a topology with fixed volume a higher number of pores increases growth rates. This observation is supported by the FXBC having the fastest growth since it has the high-

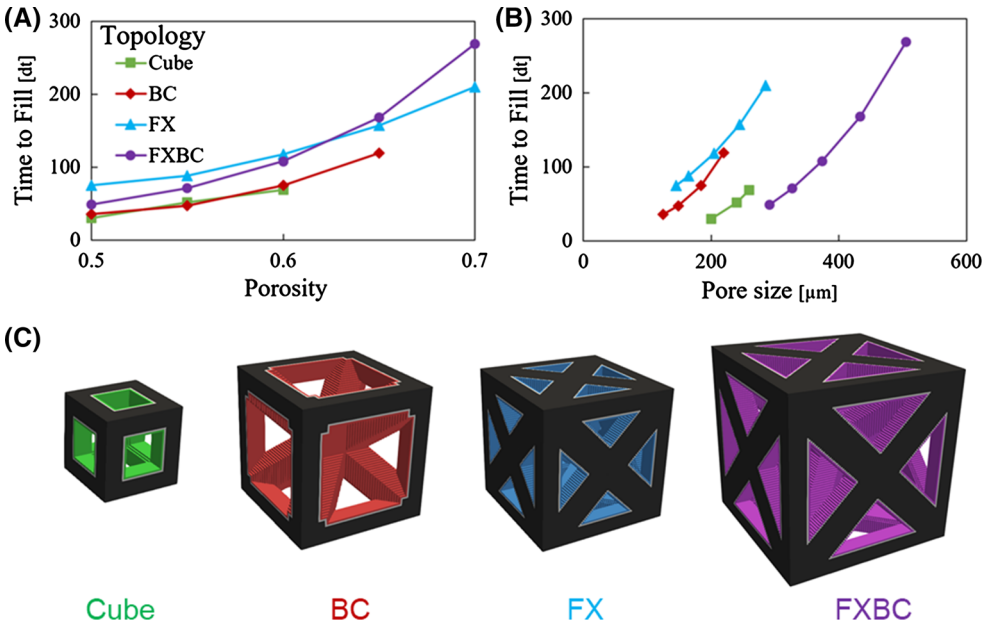

Fig. 7 Time steps to fill t_{fill} for designs of **a** porosity P and **b** pore size p with beam width $w = 200\,\mu\text{m}$. **c** Seeded unit cell renderings when $P = 0.6$ that illustrate the relative unit cell sizes across topologies

est number of planar pores initially and three spherical pores toward the end of the filling process.

Although the FX topology has a higher surface–volume ratio than the BC topology, it fills at a lower overall rate due to the large central void that forms and slows growth, even though it has a higher amount of seeded tissue. Therefore, it is not always obvious which structure facilitates the fastest tissue growth across topologies based on seeded tissue volume alone, which motivates the need for investigating further cases when volume is not fixed. Simulations with fixed beam width $w = 200\,\mu\text{m}$ were conducted, resulting in comparison with fixed porosity P from $P = 0.5$ to $P = 0.7$ in 0.05 increments by adjusting unit cell length l (Fig. 7; Supplementary Movie 4); note these porosities refer to the structural porosity prior to tissue seeding.

As porosity and pore size increase, there is an increasingly longer time required to fill any topology (Fig. 7). The Cube and BC topologies have similar growth rates for a given porosity, but different pore sizes. This difference suggests that pore size is not a reliable predictor of tissue growth rates when comparing across topologies. In contrast to Fig. 6 results, when the FXBC topology filled fastest, the Cube and BC topologies fill the fastest for a given porosity when beam width is fixed. Fixing beam width is potentially of interest due to manufacturing limitations. The fast growth of the Cube topology occurs due to its small unit cell volume relative to the other topologies for these controls. The FXBC topology fills slower due to its overall large volume and demonstrates that when considering Figs. 6 and 7 the relative trade-offs among topologies differ based on chosen comparison criteria.

A systematic analysis was conducted for diverse scaffolds, with curvature–surface ratio $\overline{\kappa_+}/S$ and surface–volume ratio S/V assumed as influential factors on tissue growth as a basis for analytically describing growth trends in relation to designed topologies, in addition to considering pore size p as a potential predictor. $\overline{\kappa_+}/S$ influences tissue growth, as demonstrated in Fig. 6, since localized tissue growth only occurs when curvature is positive while S/V determines the amount of initial tissue present, thus providing more points for potential growth. $\overline{\kappa_+}/S$ and S/V are considered simultaneously by taking their product to find the curvature–volume ratio

$$\overline{\kappa_+}/V = (\overline{\kappa_+}/S) \cdot (S/V) \tag{8}$$

that is potentially a better predictor for 3D geometries in comparison with $\overline{\kappa_+}/S$, that is useful for 2D geometries (Bidan et al. 2013).

Designs were generated by finding the ratio of beam width w to unit cell length l for each design in Fig. 5 at porosities ranging from $P = 0.5$ to $P = 0.8$ prior to tissue seeding for every 0.05 difference in porosity. Holding the ratio constant enables rescaling of structures by altering w and l while maintaining a consistent porosity (Egan et al. 2017). Geometries were generated by setting $w = 200\,\mu\text{m}$ and increasing w in $20\,\mu\text{m}$ increments while $l \leq 2000\,\mu\text{m}$ for the ratios considered. Smaller w tends to create highly porous structures that do not facilitate growth, while larger l does not facilitate

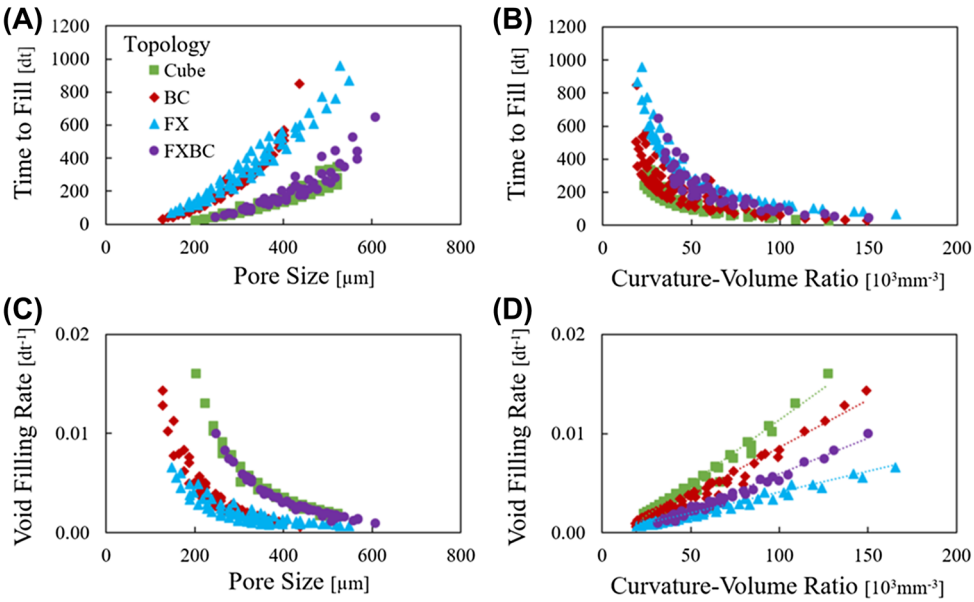

Fig. 8 **a** Time to fill t_{fill} for designs as a function of pore size p and **b** curvature–volume ratio $\overline{\kappa_+}/V$. **c** Void filling rate V_{rate} as a function of p and **d** curvature–volume ratio $\overline{\kappa_+}/V$, with dotted lines for linear regressions

fast tissue growth. Simulation results that did not converge with complete filling were not considered in these results, as their proportional void filling behavior is not consistent when comparing growth rates to simulations with complete filling. Time to fill t_{fill} as a function of p and $\overline{\kappa_+}/V$ are plotted in Fig. 8a, b, respectively.

t_{fill} increases as p increases and $\overline{\kappa_+}/V$ decreases, with trends differing for each topology. For instance, the FXBC topology has a lower t_{fill} for p relative to the FX and BC topologies, but a relatively high t_{fill} for $\overline{\kappa_+}/V$ in comparison with all other topologies. For both plots, trends show a spread of values for a given p or $\overline{\kappa_+}/V$ that are adjusted by replotting according to the void filling rate V_{rate} of

$$V_{\text{rate}} = P/t_{\text{fill}} \tag{9}$$

that provides a rate measure when factoring in P that adjusts for each unit cell having a different capacity for total tissue growth per volume. In Fig. 8c, d, V_{rate} decreases as p decreases and k/V increases, and trends appear to provide a more reliable basis for developing regression models for predicting tissue growth behavior based on scaffold geometry.

An analytical expression was fit by considering coefficients A and B for a linear regression

$$V_{\text{rate}} \approx A \cdot \overline{\kappa_+}/V + B \tag{10}$$

that agrees strongly with the data presented in Fig. 8d. Fits for each topology are unique: For the Cube topology $A = 1.3 \times 10^{-7}$, $B = -1.5 \times 10^{-3}$ $(R^2 = 0.97)$, for the BC topology $A = 9.6 \times 10^{-8}$, $B = -1.0 \times 10^{-3} (R^2 = 0.96)$, for the FX topology $A = 4.2 \times 10^{-8}$, $B = -7.0 \times 10^{-5}$ $(R^2 = 0.97)$, and for the FXBC topology $A = 7.1 \times 10^{-8}$, $B = -1.2 \times 10^{-3}$ $(R^2 = 0.98)$. These findings are summarized in Table 1.

Table 1 Summarized Fig. 8d linear regression values

Topology	A	B	R^2
Cube	1.3×10^{-7}	-1.5×10^{-3}	0.97
BC	9.6×10^{-8}	-1.0×10^{-3}	0.96
FX	4.2×10^{-8}	-7.0×10^{-5}	0.97
FXBC	7.1×10^{-8}	-1.2×10^{-3}	0.98

When using $\overline{\kappa_+}/S$ in isolation for linear regressions, $R^2 = 0.86$ to $R^2 = 0.96$ and $R^2 = 0.79$ to $R^2 = 0.96$ when considering S/V in isolation. These lower R^2 values justify the use of $\overline{\kappa_+}/V$ ratio in comparison with either of these ratios for predicting three-dimensional growth based on scaffold geometry using a linear regression.

3.4 Tissue growth and permeability trade-offs

Design maps were generated to directly relate how design parameters of beam width w and pore size p influence void filling rate V_{rate} and permeability k, that are potentially conflicting trade-offs during scaffold optimization (Kang et al. 2013; Melancon et al. 2017). Maps were generated by increasing w from 100 to 1000 μm in 20 μm increments at porosities P from 0.5 to 0.8 in 0.05 increments. Designs were configured for a specified P based on the ratio of w to unit cell length l for scaffolds prior to tissue seeding, up to $l = 2000$ μm or $p = 1000$ μm. A contour plot was generated with w and p as independent variables and void filling rate colored based on a log scaling for each topology (Fig. 9), with both complete void filling and halted

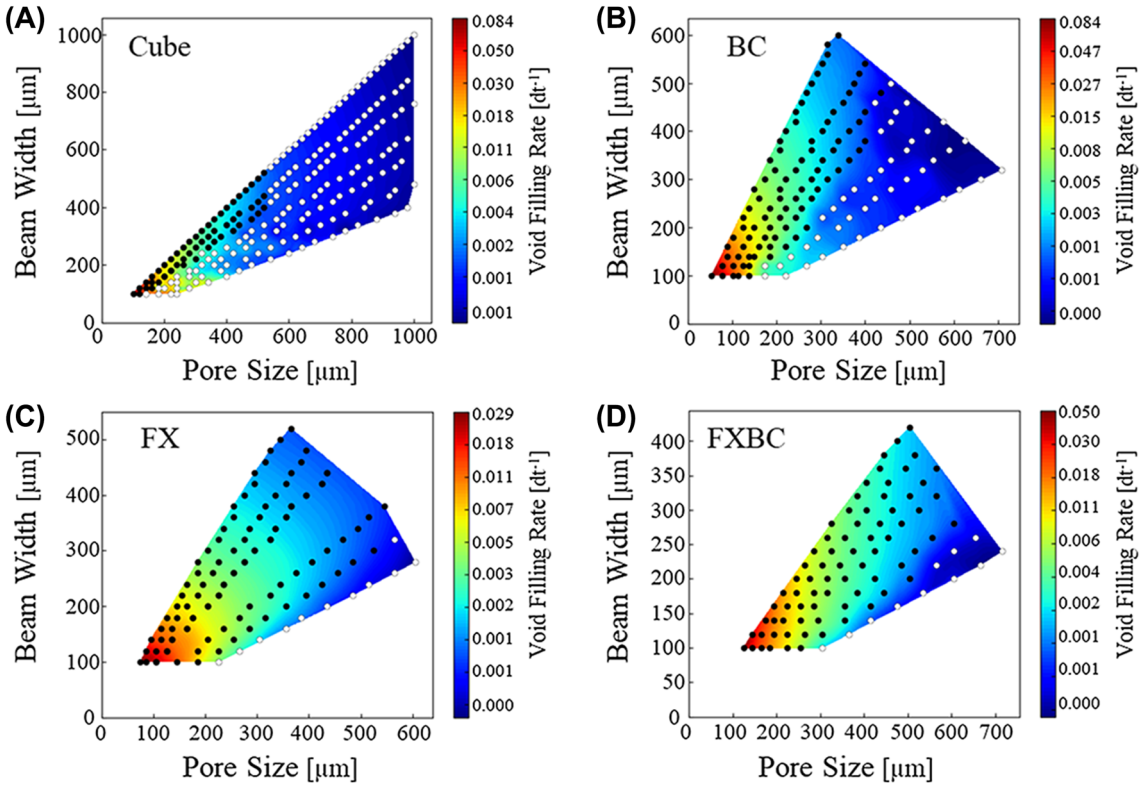

Fig. 9 Design maps for void filling rate V_{rate} as a function of beam width w and pore size p for **a** Cube **b** BC, **c** FX, and **d** FXBC topologies; circles indicate simulated designs, with open circles indicating halted growth; void filling rate is plotted using a log color scale

growth simulations plotted as discrete points. The design space revealed by each map is constrained by minimum w as a horizontal line on the bottom, maximum P as a line with positive slope on the bottom, minimum P as a line with positive slope on the top, and maximum l as a line with negative slope on the top. The Cube design map also reaches its maximum p as a vertical boundary on its right

The design maps demonstrate that as w and p decrease, V_{rate} increases, and further implies V_{rate} increases with lower P and lower l. Growth is more likely to halt as w decreases, p increases, and P increases, and supports the notion that halted growth is based on a ratio of these variables to one another rather than absolute values. Design maps were then generated for permeability k that is a measure of fluid flow through a structure and used as an estimate for how much initial nutrient transport occurs. It is calculated by considering a constant K used in the Kozeny–Carmen relation

$$k = K\frac{P^3}{(S/V)^2} \tag{11}$$

where $K = 2.75 \times 10^{-7}$ for cube topology types, based on past simulations (Egan et al. 2017). Permeability design maps were generated using the same simulation data as Fig. 9, with permeability colored based on a log scaling.

The maps suggest that k does not strongly depend on w and increases with higher p, which opposes the findings for increasing V_{rate} in Fig. 9. Additionally, permeability increases with higher P as suggested by Equation 11, while higher S/V in Equation 11 results in lower permeability that generally occurs as beams/pores decrease in size and are packed more tightly. V_{rate} and k are plotted directly against one another to better visualize their conflicting values across the design space. When V_{rate} is plotted as a function of k for each simulated design, a hyperbolic relationship emerges with higher V_{rate} generally leading to lower k (Fig. 11a).

The trade-off provides a pareto front (Blasco et al. 2008; Wilson et al. 2001) for each topology that describes the best value for a given V_{rate} for a given k, and vice versa; the highest performing designs have higher values of each of these variables and therefore are further away from the bottom-left of the plot. A pareto front is the subset of simulation data points for a topology such that it is impossible to alter a topology's design to improve one of these properties without worsening the other. A "Balanced Designs" region of Fig. 11a is indicated for pareto designs that retain high relative values of tissue growth rates while minimizing significant reductions in permeability (and vice versa) and have complete void fill-

Table 2 Parameters, properties, and tissue growth performance for selected designs in balanced region of Fig. 11a

Design parameters			Lattice properties					Performance	
Topology	Beam width	Length	Porosity	Pore size	Curvature–surface ratio	Surface–volume ratio	Permeability	Time to fill	Void filling rate
	w (μm)	l (μm)	P (−)	p (μm)	κ_+/S (10^3 mm^{-3})	S/V (mm^{-1})	κ (10^{-8} m^2)	t_{Fill} (dt)	V_{rate} (dt^{-1})
Cube	360	720	0.50	360	12	3.9	0.22	105	0.0048
BC	320	1070	0.52	196	17	3.6	0.30	96	0.0054
FX	280	1050	0.49	185	23	4.2	0.19	138	0.0036
FXBC	320	1520	0.51	385	18	3.8	0.25	130	0.0039

ing behavior. Halted growth for some Cube designs extend in a favorable region beyond the pareto front for filled scaffolds, however, they tend to have very poor proportional growth (e.g., all halted Cube designs converge with $P \geq 0.4$). Highlighted scaffolds in the balanced design region have similar properties and simulated performance quantified in Table 2 for each topology, despite having different numbers of unit cells required to fill a volume (Fig. 11b).

Findings demonstrate how diverse lattices achieve similar performance for a given application despite their differing geometries. In Table 2, topologies have a porosity of $P \approx 0.5$, resulting in the Cube topology having the smallest unit cells, while the FXBC topology has the largest. Beam width w ranges from 280 to 360 μm, which is a small range considering the entire range of beam widths considered. Generally, topologies with lower w have high surface–volume ratios that reduce permeability, while topologies with higher w have large unit cells that reduce tissue growth rate due to low curvature–volumes ratios when compared to the balanced designs. Results demonstrate the conflicting trends in tissue scaffold design and suggest there is a small range of designs for each topology that favorably satisfy these opposing trade-offs.

4 Discussion

A computational approach was developed to simulate growth of tissues that mechanically sense curvature in complex 3D structures, as a basis for investigating how designed scaffold geometry relates to tissue growth performance in beam-based scaffolds. Initial simulations compared growth in 2D/2.5D geometries to beam-based Cube topologies. Beams required a sufficient width in comparison with porous volume to ensure concave curvature is maintained in the tissue growth process, otherwise tissue growth halts. When considering topologies with varied beam topologies (Fig. 6), pore filling requires different time durations when porous volume is fixed for each topology and contrasts with 2D simulations where pore filling completes in the same duration when porous volume and void area are fixed across designs (Bidan et al. 2013). These differences may be explained by 3D cases having open porous geometries prior to growth forming closed internal pores. The contrast highlights the greater complexity in assessing growth in the 3D geometries.

Simulations were conducted systematically for four lattice topologies with diverse configuration parameters to identify trends among 3D beam-based scaffold properties. Common predictors for tissue growth rate, such as pore size and surface–volume ratio (Egan et al. 2017), were not sufficient to explain differences among topology growth rates. Trends suggest that tissue growth rate is proportional to a lattice's curvature–volume ratio, which is the product of curvature–surface ratio and surface–volume ratio that are known from past studies to coincide with tissue growth (Bidan et al. 2013). Linear regressions with A and B coefficients (Equation 10) were found for each topology and demonstrated strong fits ($R^2 \geq 0.96$), with unique coefficients for each topology. The purpose of these regressions is to find analytical equations that accurately approximate simulation outputs, but are computationally efficient for design optimization algorithms (Egan et al. 2015, 2016). Past research has found analytical regressions for mechanical properties of scaffolds and permeability, with permeability relations being used to generate data in Figs. 10 and 11 (Egan et al. 2017). A and B coefficient values are potentially representative of geometrical differences in topologies for how beams are organized to influence void filling behavior, and future work may investigate these differences as well as further regression models that accurately predict tissue growth behavior.

Design maps were then generated for linking scaffold design parameters to tissue growth and permeability outputs (Melancon et al. 2017) that are clinically relevant. Conflicting trade-offs for tissue growth rates and permeability are highlighted in Fig. 11, that demonstrated a hyperbolic trade-off that provides a pareto front (Blasco et al. 2008). Unit cell designs on the pareto front in the balanced design region of Fig. 11 have permeability values slightly lower than that of trabecular bone ($k = 1 \times 10^{-8}$ m^2) (Baroud et al. 2004; Daish et al. 2017). However, unit cells with lower permeabil-

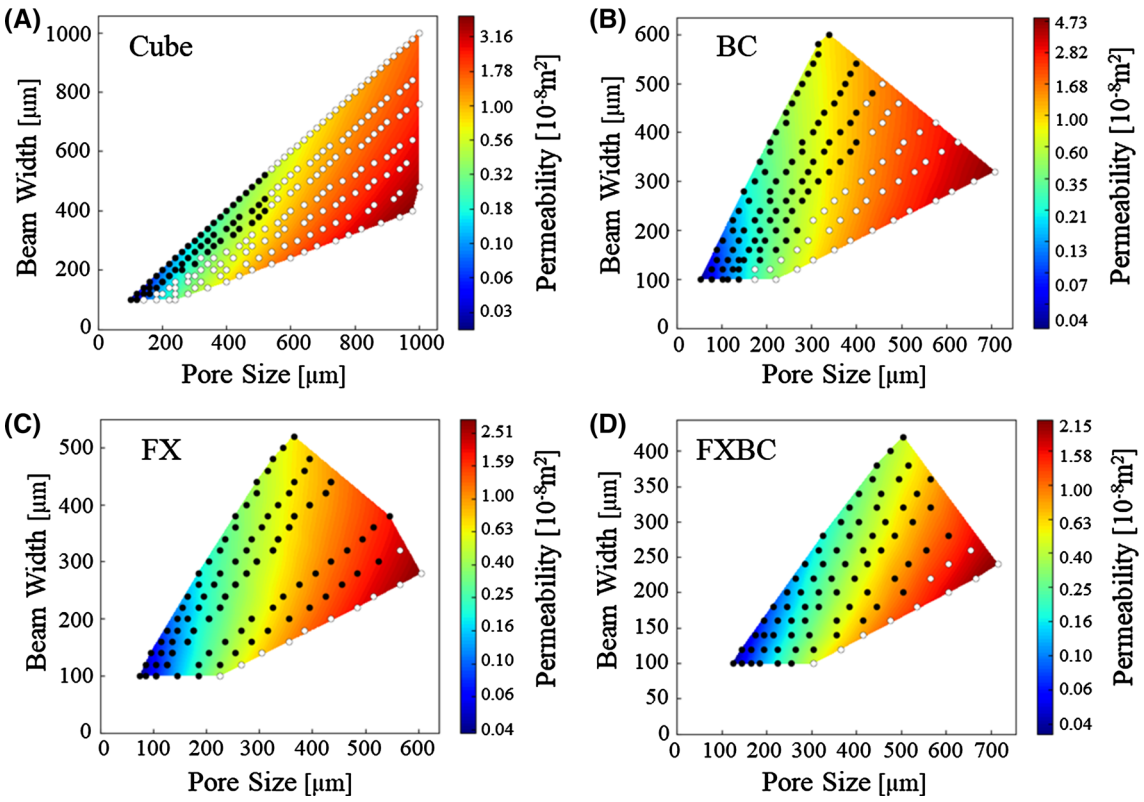

Fig. 10 Design maps for permeability k as a function of beam width w and pore size p for **a** Cube, **b** BC, **c** FX, and **d** FXBC topologies; circles indicate simulated designs, with open circles indicating halted growth; permeability is plotted using a log color scale

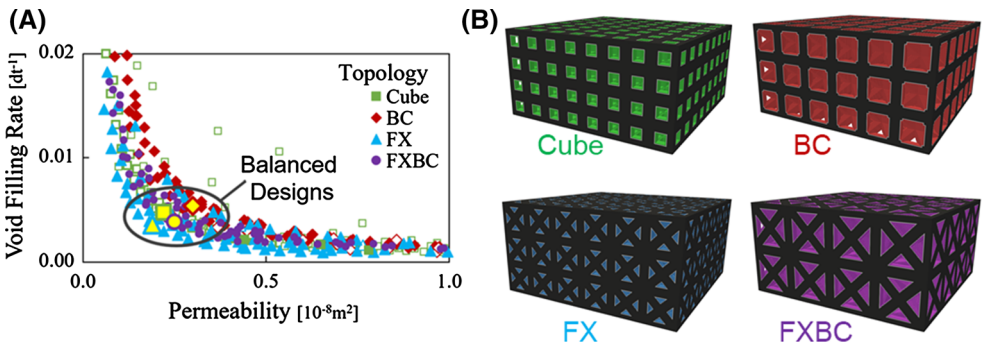

Fig. 11 **a** Void filling rate V_{rate} for diverse scaffold designs of permeability k; open symbols denote designs with halted growth. **b** Rendered scaffolds with similar nominal volumes were constructed with unit cells denoted in panel **a** by yellow symbols in "Balanced Designs" region

ity are potentially useful in scaffolds with hierarchical pores or channels for efficient nutrient transport (Egan et al. 2017). The BC scaffold achieved the highest void filling rate and permeability among selected balanced designs. However, the best topology is difficult to determine, since each topology has different tunings that are advantageous when considering further property trade-offs (Egan et al. 2017). Nevertheless, the establishment of a consistent growth rate/permeability balance point with varying scaffold topologies implies that a subsequent mechanical optimization is possible, with target values of structural properties governing the final topology selection.

There are also inherent limitations in modeling approaches that could influence design choice, such as the symmetry assumptions for growth representing a best-case scenario for uniform growth based on a lack of data to reliably consider how heterogeneous cell density and variable growth rates are influenced by scaffold geometry. The simulation approach used a voxel environment that introduces numerical error, such as approximating curvature with a discretized scanning mask rather than a continuous sphere. Increasing mask res-

olution provides a closer approximation to an ideal sphere, but increases computational costs as overall environment size is rescaled due to the mask radius representing the physical reach of a cell, in addition to having more voxels in the mask considered for curvature calculations. Increasing mask size was demonstrated to have diminishing improvements in efficiency (Fig. 4), since higher resolution masks require greater computational time but do not significantly influence simulation outcomes. Further difficulties in matching simulation to experiment emerge when considering the uncertainty in how far cells reach when mechanically sensing their environment that could also account for differences in modeled and actual growth. Improvements in computational time are potentially possible through efficient ways of estimating curvature (Kronenberger et al. 2015; Batagelo and Wu 2007). Additionally, adjusting mask size during the simulation could reduce curvature over-estimation as pores are closing; mask size adjustment requires rescaling the environment size to retain physical relevance in representing a fixed cell reach distance for the mask. Relevant simulation assumptions may require further tuning to retain accuracy and efficiency when considering differently shaped beams or novel topologies.

To assess differences in discretized and continuous environments, a Cube unit cell was generated with beam width $w = 120\,\mu\text{m}$ and unit cell length $l = 620\,\mu\text{m}$ using a discretized approach that provides porosity $P = 0.90$, surface–volume ratio $S/V = 3.0\,\text{mm}^{-1}$, and permeability $k = 2.23 \times 10^{-8}\,\text{m}^2$, while evaluations from a continuous modeling approach provide $P = 0.91$, surface–volume ratio $S/V = 2.6\,\text{mm}^{-1}$, and permeability $k = 3.07 \times 10^{-8}\,\text{m}^2$ (Egan et al. 2017). Both models have similar values for porosity but differ by about 15% for surface–volume ratio, although the higher estimation from the discretized environment may better account for the rough surface of 3D printed parts (Arabnejad et al. 2016). Further experimental work is required to fully understand how tissues grow as a result of differences in geometry and complexity on 3D printed surfaces and are necessary to fully validate the simulation for optimization of scaffolds for clinical applications. When considering beam cross sections, extrusion-based 3D printing processes are typically used to fabricate scaffold beams with circular cross sections that correspond with the shape of extrusion at their minimum printable dimensions. A circular cross section would lead to overall slower growth due to greater convex curvature in comparison with square cross sections that are achievable with stereolithography and polyjet processes at microscales.

Property predictions are also sensitive to the modeling approach used, and adjustments could enable higher accuracy or inclusion of further phenomenon influencing tissue growth such as mechanotransduction, fluid shear stress, and vascularization that also influence tissue growth (Czarnecki et al. 2014; Garijo et al. 2012; Gardiner et al. 2015; Carlier et al. 2012; Byrne et al. 2007; Boccaccio et al. 2016). Simulations using level set curvature-based methods have demonstrated a strong match to in vitro growth when considering the spatial distribution of tissues for a small sample of 3D printed scaffolds, however, there is difficulty in matching predictions to the culture time (Guyot et al. 2014). Past models using a voxel environment for assessing curvature have found a fit of approximately 12 time steps representing one day of culture time (Bidan et al. 2013). Our simulation's time step is estimated for Saos-2 tissue growth by considering the in vitro data in Fig. 1 for the FXBC scaffold designed with beam width $w = 500\,\mu\text{m}$ and unit cell length $l = 2200\,\mu\text{m}$. In Fig. 1d, the growth for the planar pore, imaged using confocal microscopy after 35 days of cell culture, is about 50–80% filled for an FXBC scaffold. In the simulation of the fabricated scaffold, the triangular pore fills 50% of its planar area at step 96 and 80% at step 126, thus suggesting that 3 simulation steps represent one day in cell culture. Further experimental studies are required to fully validate the simulation due to stochasticity of in vitro experiments and limited data.

There is a need for further experiments to fully characterize how curvature-based growth occurs in a variety of scaffolds of different topologies and materials, in addition to characterization for varied cell types and animal models. Recent experiments for in vivo tissue growth have demonstrated growth halting on a scaffold with a topology similar to the Cube topology, constructed with extrusion processes with 300 μm beam width and 1200 μm unit cell length (Paris et al. 2017). The halting behavior supported bone mineralization and suggests the need for further studies to investigate the absolute amount of tissue that forms and can facilitate bone growth once tissue growth halts.

Tantalum foam is an alternate material that has been successfully used for tissue engineering (Zardiackas et al. 2001), with beam diameters of 100 μm and pore sizes of 700 μm. When these design parameters are used to generate beam-based designs, it typically results in halted growth (Fig. 9). Void filling growth may occur for tantalum foams due a different surface finish, local material properties, planar pores having greater concave curvature, or a stochastic distribution in pore sizes such that small pores stimulate initial tissue growth throughout the structure. Future work in both modeling and experiments is necessary to identify the most favorable scaffold designs for clinical applications. Due to the large number of factors that influence performance, development of further computational methods is crucial for informing experimental endeavors and tuning high-performance scaffolds.

5 Conclusion

Simulations were developed for assessing tissue growth based on cells mechanically sensing their environment in 3D printed scaffolds. When comparing topologies with fixed porosity and unit cell size, unit cells with the most beams had the highest tissue growth rate while unit cells with fewer beams had the highest growth rate when beam width and porosity were fixed across topologies. A linear regression was developed by fitting the void filling rate of a scaffold to its curvature–volume ratio, thus enabling estimation of tissue growth rates based solely on geometric scaffold properties. Design maps were generated that linked scaffold design parameters to tissue growth rate and permeability properties, demonstrating conflicting trade-offs. Scaffolds with higher tissue growth rates tended to have lower permeabilities, with a balance found for scaffolds with beam diameters of about 300 μm and 50% porosity. These findings highlight the need to tune scaffold designs through careful consideration of all factors relevant to clinical applications, and provide quantitative results for assessing potential tissue growth rates based on substrate curvature.

Acknowledgements Karin Würtz-Kozak and Helen Greutert aided with in vitro experiments and imaging.

Compliance with ethical standards

Conflict of interest The authors declare that they have no conflict of interest.

References

Alias MA, Buenzli PR (2017) Modeling the effect of curvature on the collective behavior of cells growing new tissue. Biophys J 112:193–204

Arabnejad S, Johnston RB, Pura JA, Singh B, Tanzer M, Pasini D (2016) High-strength porous biomaterials for bone replacement: a strategy to assess the interplay between cell morphology, mechanical properties, bone ingrowth and manufacturing constraints. Acta Biomater 30:345–356

Baroud G, Falk R, Crookshank M, Sponagel S, Steffen T (2004) Experimental and theoretical investigation of directional permeability of human vertebral cancellous bone for cement infiltration. J Biomech 37:189–196

Batagelo HC, Wu S-T (2007) Estimating curvatures and their derivatives on meshes of arbitrary topology from sampling directions. Vis Comput 23:803–812

Bidan CM, Kommareddy KP, Rumpler M, Kollmannsberger P, Bréchet YJ, Fratzl P, Dunlop JW (2012) How linear tension converts to curvature: geometric control of bone tissue growth. PLoS ONE 7:e36336

Bidan CM, Wang FM, Dunlop JW (2013) A three-dimensional model for tissue deposition on complex surfaces. Comput Methods Biomech Biomed Eng 16:1056–1070

Bidan CM, Kommareddy KP, Rumpler M, Kollmannsberger P, Fratzl P, Dunlop JW (2013) Geometry as a factor for tissue growth: towards shape optimization of tissue engineering scaffolds. Adv Healthc Mater 2:186–194

Bischofs IB, Schwarz US (2003) Cell organization in soft media due to active mechanosensing. Proc Natl Acad Sci 100:9274–9279

Blasco X, Herrero JM, Sanchis J, Martínez M (2008) A new graphical visualization of n-dimensional Pareto front for decision-making in multiobjective optimization. Inf Sci 178:3908–3924

Boccaccio A, Uva AE, Fiorentino M, Lamberti L, Monno G (2016) A mechanobiology-based algorithm to optimize the microstructure geometry of bone tissue scaffolds. Int J Biol Sci 12:1

Buenzli PR (2016) Governing equations of tissue modelling and remodelling: a unified generalised description of surface and bulk balance. PLoS ONE 11:e0152582

Bullard J, Garboczi E, Carter W, Fuller E (1995) Numerical methods for computing interfacial mean curvature. Comput Mater Sci 4:103–116

Byrne DP, Lacroix D, Planell JA, Kelly DJ, Prendergast PJ (2007) Simulation of tissue differentiation in a scaffold as a function of porosity, Young's modulus and dissolution rate: application of mechanobiological models in tissue engineering. Biomaterials 28:5544–5554

Carlier A, Geris L, Bentley K, Carmeliet G, Carmeliet P, Van Oosterwyck H (2012) MOSAIC: a multiscale model of osteogenesis and sprouting angiogenesis with lateral inhibition of endothelial cells. PLoS Comput Biol 8:e1002724

Carlier A, Geris L, Lammens J, Van Oosterwyck H (2015) Bringing computational models of bone regeneration to the clinic. Wiley Interdiscip Rev Syst Biol Med 7:183–194

Christen P, Schulte FA, Zwahlen A, Van Rietbergen B, Boutroy S, Melton LJ, Amin S, Khosla S, Goldhahn J, Müller R (2016) Voxel size dependency, reproducibility and sensitivity of an in vivo bone loading estimation algorithm. J R Soc Interface 13:20150991

Czarnecki JS, Jolivet S, Blackmore ME, Lafdi K, Tsonis PA (2014) Cellular automata simulation of osteoblast growth on microfibrous-carbon-based scaffolds. Tissue Eng Part A 20:3176–3188

Daish C, Blanchard R, Gulati K, Losic D, Findlay D, Harvie D, Pivonka P (2017) Estimation of anisotropic permeability in trabecular bone based on microCT imaging and pore-scale fluid dynamics simulations. Bone Rep 6:129–139

de Wild M, Zimmermann S, Rüegg J, Schumacher R, Fleischmann T, Ghayor C, Weber FE (2016) Influence of microarchitecture on osteoconduction and mechanics of porous titanium scaffolds generated by selective laser melting. 3D Print Addit Manuf 3:142–151

Egan P, Moore J, Schunn C, Cagan J, LeDuc P (2015) Emergent systems energy laws for predicting myosin ensemble processivity. PLoS Comput Biol 11:e1004177

Egan P, Cagan J, Schunn C, Chiu F, Moore J, LeDuc P (2016) The D3 methodology: bridging science and design for bio-based product development. J Mech Des 138:081101

Egan PF, Gonella VC, Engensperger M, Ferguson SJ, Shea K (2017) Computationally designed lattices with tuned properties for tissue engineering using 3D printing. PLoS ONE 12:e0182902

Egan P, Ferguson S, Shea K (2017) Design of hierarchical three-dimensional printed scaffolds considering mechanical and biological factors for bone tissue engineering. J Mech Des 139:1–9

Frette OI, Virnovsky G, Silin D (2009) Estimation of the curvature of an interface from a digital 2D image. Comput Mater Sci 44:867–875

Fyhrie DP, Fazzalari N, Goulet R, Goldstein SA (1993) Direct calculation of the surface-to-volume ratio for human cancellous bone. J Biomech 26:955–967

Gardiner BS, Wong KK, Joldes GR, Rich AJ, Tan CW, Burgess AW, Smith DW (2015) Discrete element framework for modelling extracellular matrix, deformable cells and subcellular components. PLoS Comput Biol 11:e1004544

Garijo N, Manzano R, Osta R, Perez M (2012) Stochastic cellular automata model of cell migration, proliferation and differentia-

tion: validation with in vitro cultures of muscle satellite cells. J Theor Biol 314:1–9
Guyot Y, Papantoniou I, Chai YC, Van Bael S, Schrooten J, Geris L (2014) A computational model for cell/ECM growth on 3D surfaces using the level set method: a bone tissue engineering case study. Biomech Model Mechanobiol 13:1361–1371
Guyot Y, Luyten F, Schrooten J, Papantoniou I, Geris L (2015) A three-dimensional computational fluid dynamics model of shear stress distribution during neotissue growth in a perfusion bioreactor. Biotechnol Bioeng 112:2591–2600
Guyot Y, Smeets B, Odenthal T, Subramani R, Luyten FP, Ramon H, Papantoniou I, Geris L (2016a) Immersed boundary models for quantifying flow-induced mechanical stimuli on stem cells seeded on 3D scaffolds in perfusion bioreactors. PLoS Comput Biol 12:e1005108
Guyot Y, Papantoniou I, Luyten F, Geris L (2016b) Coupling curvature-dependent and shear stress-stimulated neotissue growth in dynamic bioreactor cultures: a 3D computational model of a complete scaffold. Biomech Model Mechanobiol 15:169–180
Hollister SJ, Flanagan CL, Zopf DA, Morrison RJ, Nasser H, Patel JJ, Ebramzadeh E, Sangiorgio SN, Wheeler MB, Green GE (2015) Design control for clinical translation of 3D printed modular scaffolds. Ann Biomed Eng 43:774–786
Joly P, Duda GN, Schöne M, Welzel PB, Freudenberg U, Werner C, Petersen A (2013) Geometry-driven cell organization determines tissue growths in scaffold pores: consequences for fibronectin organization. PLoS ONE 8:e73545
Kang H, Hollister SJ, La Marca F, Park P, Lin C-Y (2013) Porous biodegradable lumbar interbody fusion cage design and fabrication using integrated global–local topology optimization with laser sintering. J Biomech Eng 135:101013
Knychala J, Bouropoulos N, Catt C, Katsamenis O, Please C, Sengers B (2013) Pore geometry regulates early stage human bone marrow cell tissue formation and organisation. Ann Biomed Eng 41:917–930
Kronenberger M, Wirjadi O, Freitag J, Hagen H (2015) Gaussian curvature using fundamental forms for binary voxel data. Graph Models 82:123–136
Liu Q, Li J, Liu J (2017) ParaView visualization of Abaqus output on the mechanical deformation of complex microstructures. Comput Geosci 99:135–144
Melancon D, Bagheri Z, Johnston R, Liu L, Tanzer M, Pasini D (2017) Mechanical characterization of structurally porous biomaterials built via additive manufacturing: experiments, predictive models, and design maps for load-bearing bone replacement implants. Acta Biomater 63:350–368
Melchels FP, Bertoldi K, Gabbrielli R, Velders AH, Feijen J, Grijpma DW (2010) Mathematically defined tissue engineering scaffold architectures prepared by stereolithography. Biomaterials 31:6909–6916
Papachroni KK, Karatzas DN, Papavassiliou KA, Basdra EK, Papavassiliou AG (2009) Mechanotransduction in osteoblast regulation and bone disease. Trends Mol Med 15:208–216
Paris M, Götz A, Hettrich I, Bidan CM, Dunlop JW, Razi H, Zizak I, Hutmacher DW, Fratzl P, Duda GN (2017) Scaffold curvature-mediated novel biomineralization process originates a continuous soft tissue-to-bone interface. Acta Biomater 60:64–80
Rodan SB, Imai Y, Thiede MA, Wesolowski G, Thompson D, Bar-Shavit Z, Shull S, Mann K, Rodan GA (1987) Characterization of a human osteosarcoma cell line (Saos-2) with osteoblastic properties. Cancer Res 47:4961–4966
Rumpler M, Woesz A, Dunlop JW, van Dongen JT, Fratzl P (2008) The effect of geometry on three-dimensional tissue growth. J R Soc Interface 5:1173–1180
Sanz-Herrera J, Garcia-Aznar J, Doblare M (2008) A mathematical model for bone tissue regeneration inside a specific type of scaffold. Biomech Model Mechanobiol 7:355–366
Sanz-Herrera JA, Moreo P, García-Aznar JM, Doblaré M (2009) On the effect of substrate curvature on cell mechanics. Biomaterials 30:6674–6686
Sobral JM, Caridade SG, Sousa RA, Mano JF, Reis RL (2011) Three-dimensional plotted scaffolds with controlled pore size gradients: effect of scaffold geometry on mechanical performance and cell seeding efficiency. Acta Biomater 7:1009–1018
Taniguchi N, Fujibayashi S, Takemoto M, Sasaki K, Otsuki B, Nakamura T, Matsushita T, Kokubo T, Matsuda S (2016) Effect of pore size on bone ingrowth into porous titanium implants fabricated by additive manufacturing: an in vivo experiment. Mater Sci Eng C 59:690–701
Thompson MK, Moroni G, Vaneker T, Fadel G, Campbell RI, Gibson I, Bernard A, Schulz J, Graf P, Ahuja B (2016) Design for additive manufacturing: trends, opportunities, considerations, and constraints. CIRP Ann Manuf Technol 65:737–760
Van Bael S, Chai YC, Truscello S, Moesen M, Kerckhofs G, Van Oosterwyck H, Kruth J-P, Schrooten J (2012) The effect of pore geometry on the in vitro biological behavior of human periosteum-derived cells seeded on selective laser-melted Ti6Al4V bone scaffolds. Acta Biomater 8:2824–2834
Vassaux M, Milan J (2017) Stem cell mechanical behaviour modelling: substrate's curvature influence during adhesion. Biomech Model Mechanobiol 16:1–14
Vetsch JR, Müller R, Hofmann S (2016) The influence of curvature on three-dimensional mineralized matrix formation under static and perfused conditions: an in vitro bioreactor model. J R Soc Interface 13:20160425
Vossenberg P, Higuera G, Van Straten G, Van Blitterswijk C, Van Boxtel A (2009) Darcian permeability constant as indicator for shear stresses in regular scaffold systems for tissue engineering. Biomech Model Mechanobiol 8:499–507
Wang X, Xu S, Zhou S, Xu W, Leary M, Choong P, Qian M, Brandt M, Xie YM (2016) Topological design and additive manufacturing of porous metals for bone scaffolds and orthopaedic implants: a review. Biomaterials 83:127–141
Wilson B, Cappelleri D, Simpson TW, Frecker M (2001) Efficient Pareto frontier exploration using surrogate approximations. Optim Eng 2:31–50
Worley K, Certo A, Wan LQ (2013) Geometry–force control of stem cell fate. BioNanoScience 3:43–51
Zadpoor AA (2015) Bone tissue regeneration: the role of scaffold geometry. Biomater Sci 3:231–245
Zardiackas LD, Parsell DE, Dillon LD, Mitchell DW, Nunnery LA, Poggie R (2001) Structure, metallurgy, and mechanical properties of a porous tantalum foam. J Biomed Mater Res Part A 58:180–187
Zhao F, Vaughan TJ, Mcnamara LM (2015) Multiscale fluid–structure interaction modelling to determine the mechanical stimulation of bone cells in a tissue engineered scaffold. Biomech Model Mechanobiol 14:231–243